# Compromise between magnetic shielding and mechanical strength of thin Al/Steel/Al sandwiches produced by cold roll bonding: Experimental and numerical approaches

Paul Clérico, Xavier Mininger, L. Prevond, T. Baudin, A.L. Helbert

▶ To cite this version:

Paul Clérico, Xavier Mininger, L. Prevond, T. Baudin, A.L. Helbert. Compromise between magnetic shielding and mechanical strength of thin Al/Steel/Al sandwiches produced by cold roll bonding: Experimental and numerical approaches. Journal of Alloys and Compounds, 2019, 798, pp.67-81. ⟨10.1016/j.jallcom.2019.05.243⟩. ⟨hal-02359745⟩

HAL Id: hal-02359745

https://hal.science/hal-02359745v1

Submitted on 6 Dec 2019

# Compromise between magnetic shielding and mechanical strength of thin Al/Steel/Al sandwiches produced by cold roll bonding: experimental and numerical approaches

P. Clérico[a,b,c,*], X. Mininger[b], L. Prévond[c], T. Baudin[a], A.L. Helbert[a]

[a] *ICMMO, SP2M, Univ. Paris-Sud, Université Paris-Saclay, UMR CNRS 8182, bât.410, 91405 Orsay, France*
[b] *GeePs, CNRS, CentraleSupélec, Univ. Paris-Sud, Université Paris-Saclay, Sorbonne Université, 3&11 rue Joliot-Curie, Plateau de Moulon 91192 Gif-sur-Yvette CEDEX, France*
[c] *SATIE-Cnam, ENS Paris Saclay, Univ. Paris-Sud, UMR CNRS 8029, 94235 Cachan, France*

## Abstract

Electromagnetic pollution become an issue these last years with growth of electrical and electronic industry. The shielding of electromagnetic fields is one solution to reduce effects of this pollution. This study proposes an Al/Steel/Al sandwich produced by cold roll bonding to shield low frequency magnetic wave in near field. The structure evolution of sandwich composite has been characterized in function of the reduction rate of thickness. The bonding quality of Al/Steel interfaces has been then quantified by Tensile Bond Strength Test. Finally, the magnetic shielding effectiveness of the composite and the initial Al and steel sheets have been evaluated experimentally and numerically. During cold roll bonding, plastic instability has been observed and causes steel necking and fragmentation. A numerical model has been developed to explain its origin. A good bond quality is attained when debonding of Al/Steel interfaces requires the deterioration of the composite. The composite takes both shielding behavior of steel and Al and can shield low frequency. However, steel fragmentation has a negative impact on shielding effectiveness. The optimal condition between shielding and mechanical properties is then obtained for a reduction rate of 62 % where only few fragmentations are observed.

*Keywords:* Magnetic shielding effectiveness, Low frequency, Near field, Metal sandwich, Cold roll bonding, Tensile bond strength

## 1. Introduction

The observed growth of electrical and electronic industry led to the increase of electromagnetic pollution, which can cause disturbance to sensitive electrical and electronic devices [1] and can be harmful to health of human beings [2–4]. Thus, recent directives and technical standards impose its diminution. Living and critical components must then be protected from electric and magnetic fields, and electronic devices have to confine them. This can be achieved thanks to electromagnetic shielding.

---

[*] Corresponding author.
*Email address:* paul.clerico@u-psud.fr (Paul Clérico)

Most common materials for electromagnetic shields are metals [5, 6] and carbons [7, 8]. However, lightweight materials, especially required in transportation industry led to the development of composite materials. Metal and carbon reinforced polymer composites have been greatly studied in bulk or in foam form [9–12]. Multilayer composite is also an effective mean to shield [13, 14]. Nevertheless, polymers are insulating and polymer composites show lower electrical conductivity than metals bulk.

The shielding effectiveness (SE) of a material is linked to its properties, its geometry and electromagnetic wave frequency. Electrical conductivity and magnetic permeability are properties directly linked to the shielding of electromagnetic waves. First shielding theory has been proposed by Shelkunoff by using an impedance concept [15]. Impedance of a material is proportional to the ratio of its magnetic permeability $\mu$ divided by its electrical conductivity σ. Furthermore, Shelkunoff described three mechanisms contributing to the shielding of electromagnetic waves: absorption (A), reflection (R) and multiple reflections (B). Then, shielding effectiveness is defined by $SE = A + R + B$. Due to their high conductivity, aluminum (Al), gold (Au) and copper (Cu) are excellent for reflection. Steels with high permeability are good for absorption. Absorption is predominant at high frequencies and reflection is at low frequencies. Multiple reflections are negligible at high frequencies when the skin depth is small compared to the distance between reflecting interfaces.

This study proposes to determine the SE of a multilayer metal composite: Al/Steel/Al. Assembly of an Al sheet with a steel sheet is not an easy task and has been the origin of a patent [16]. By its composition and design, a good SE is expected at low and high frequencies. This study is only focused on the shielding of a magnetic wave in near field in the range [1 Hz; 10 kHz]. Low frequency magnetic fields can cause noise and disturbance to sensitive devices and are generally emitted by power supplies, switches and motors for example. A magnetic shielding is then necessary such as enclosure [17] to protect sensitive electronics from perturbations or to isolate these sources and so reduce their effect.

A thin Al/Steel/Al sandwich is produced by cold roll bonding (CRB). CRB is a well-known method of metal forming where metals can be mechanically bonded by rolling at room temperature [18–20]. Quality of the bond is dependent on several parameters extrinsic and intrinsic of rolling [21–23]. Reduction rate of the thickness, size and rotation speed of rolls, coefficient of friction between the sample and rolls can be cited. Layer thickness, surface condition and pre- and post-annealing also affect the bond quality. Optimal bonding can be achieved with higher reduction rate and friction coefficient [24, 25], lower rotation speed [26], clean and brushed intimate surfaces [27, 28]. Pre-annealing generally diminishes the work-hardening effect and increases the formability allowing a better bond strength. Post-annealing can create intermetallic at the interface which is brittle and then negative to bond quality [29].

In this work, to achieve the shielding of a low frequency magnetic field, a thin metal composite based on aluminum and steel is proposed. An experimental and numerical approach is both considered from the composite production to the study of its magnetic shielding. Furthermore, mechanical strength of Al/Steel/Al composite must be ensured thanks to a good bond quality of Al/Steel interfaces to avoid any potential delamination. Then, thin Al/Steel/Al sandwiches are produced by CRB at different reduction rate. Firstly, the structure evolution is characterized by optical observation. Numerical simulation of CRB is developed to explain origins of this structure evolution. Bond quality of Al/Steel interfaces is then quantified by tensile bond strength test (TBST). The magnetic shielding properties of these multilayered composites is finally investigated experimentally and numerically at low frequencies (1 Hz - 10 kHz), and the effect of the structure on SE is evaluated. In the end, optimal condition between mechanical properties and magnetic shielding is determined.

## 2. Materials and methods

### *2.1 Materials*

Commercial low carbon steel DC01 and 8011-aluminum alloy with respectively a thickness of 100 µm and 250 µm are chosen as the raw materials. Thin raw materials are considered to produce thin composites which promote their applications in transportation and electronic industries. Volume ratio $R_{vol}$ is defined by steel volume divided by total volume, initial $R_{vol}$ is equal to 1/6. Chemical compositions of these two sheets are listed in Table 1. DC01 steel is mainly used for drawing and forming applications. 8011-aluminum is a Fe and Si based aluminum alloy which is widely used in industry. Figure 1 shows the schematic diagram of CRB process following rolling-normal cross-section (RD-ND). Both Al and steel sheets are firstly cut in rectangular shape of 1x5 $cm^2$. Samples are then cleaned in an acetone bath to eliminate grease and contaminants in the surface. Al and steel sheets are annealed in a tubular furnace respectively at 600 °C during 30 min and 5 min. These annealing conditions, inspired by [16], are used to increase malleability of Al and steel sheets. Steel surfaces are then manually prepared with a rotating stainless-steel brush with wires diameter of 0.2 mm. The brushing direction follows the rolling direction (RD). Samples are cleaned again in an acetone bath before stacking in Al/Steel/Al disposition. CRB experiments are carried out with no lubricant by using a laboratory mill (FSM 130 Durston rolling mills). The roll diameter is 65 mm and the rolling speed is around 12 mm/s. Stacked Al/Steel/Al samples are rolled consecutively using rolling reductions between 48 % and 77.5 %.

[Table 1 about here.]

[Figure 1 about here.]

### *2.2 Experimental observation*

Structural evolution due to plastic instabilities is then studied by optical observations. Dissolution of Al layers is performed in a concentrated NaOH bath to analyze the structure of the steel layer after CRB. After total dissolution of Al, steel layer is scanned with opaque and film modes to reveal plastic instability. RD-ND cross-section of Al/Steel/Al composite is polished using P800-P4000 grit sand papers, finalized with 3 and 1µm alumina particles and investigated by optical microscopy. Plastic instability is a known phenomenon in rolling, especially in accumulative roll bonding when the harder phase is fragmented in the softer phase [30]. However, plastic instability has rarely been observed with only one pass of a tri-layer composite. Previously, Hwang et al. [31] have defined theoretical criteria of diffusion necking and local necking and Reihanian et al. [32] have defined a theoretical criterion of fragmentation during rolling. These criteria depend on the thickness ratio and the mechanical properties of each layers and are achieved from a certain reduction rate. However, these predicted criteria are in many cases much lower than that observed by the experiments due to strong hypotheses [32]. In our case, the predicted criterion of fragmentation based on [32] is for a reduction rate of only 13 %. The brushed steel that shows a very low strain-hardening coefficient partially explains this result.

### 2.3 *Numerical approach for cold roll bonding*

In a complementary effort to understand plastic instability origin, non-steady-state numerical simulations of CRB are developed using a commercial finite element software ANSYS (v17.2). 2D plane strain condition without lateral spreading is assumed. Al/Steel/Al sandwich with 600 µm total thickness and 10 mm length has been considered. Each layer is composed of around 7000 quadratic eight-noded elements. Rolls are assumed rigid and then only their surfaces are meshed by around 2000 elements. Plastic behavior of both steel and Al layers are represented by a power law $\sigma = K\epsilon^n$ extrapolated from experimental tensile test curve of annealed Al sheet and annealed-brushed steel sheet (Figure 2). Plastic behavior extrapolation is realized from $R_{p0,2}$ to $R_m$ of experimental curve. The strength coefficient $K$ and the strain-hardening exponent $n$ are 512.9 MPa and 0.024 for steel sheet and 219.5 MPa and 0.265 for Al sheet. The brushing generates a low strain-hardening exponent of steel. Friction between rolls and Al/Steel/Al strip and between Al and steel layers are considered respectively with a coefficient of 0.1 and 0.6. A low coefficient between rolls and strip is chosen to facilitate simulation convergence. A higher coefficient is considered between Al and steel sheets to simulate the steel brushing influence and the resulting roughness. Friction is modeled with an augmented Lagrange formulation. A lower rolling speed than experimental one is used to restrict mesh distortion. Numerical CRB is conducted with different reduction rate r = 50, 60 and 70 %.

[Figure 2 about here.]

### 2.4 *Tensile Bond Strength Test*

The bond quality is usually measured by a peeling test. However, due to the low thickness of Al/Steel/Al strip, Al layer tends to be torn during peeling test. Furthermore, peeling angle tends to increase distorting bond strength. Peeling test is then not relevant for low thickness Al/Steel/Al multilayer. In this study, the bond quality was measured by a tensile bond strength test (TBST). Figure 3 shows the schematic diagram of the TBST process. Composite samples are glued between two bars of aluminum. Surfaces in contact are first cleaned in an acetone bath and shot-peened to increase contact area. Epoxy resin Delomonopox AD286 is used as glue in this process. Its commercial tensile strength is 64 MPa for a thickness of 2 mm after a curing time of 40 min at 150 °C. No microstructural change of Al and steel sheets is observed after curing. Tensile test is then realized until reaching the bond interface breaking with a 2 mm/min speed applied by a Zwick Roell XForce P 10 kN. Engineering stress-strain curve attain a maximum which is the tensile bond strength (TBS). TBST is conducted for different rolling reduction on square samples (1.5x1.5 $cm^2$). This technique is however limited by the tensile strength of the glue, quantification of bond quality for higher reduction rate is not possible.

[Figure 3 about here.]

### 2.5 *Magnetic shielding*

Magnetic shielding effectiveness ($SE_H$) of Al/Steel/Al has been studied experimentally and numerically. Figure 4 shows the magnetic shielding measurement principle (a) and the geometry of the 3D finite element model (b). 100 copper wire turns coil of 18.5 mm height, 7.5 mm internal radius and 15 mm outer radius is used to generate the magnetic field. The coil is alimented by a low frequency generator with a 2 A current. Current density in the coil is then around $1.44 \times 10^6$ A/m².

Shielding samples are 3x3 $cm^2$ square samples and are placed 6 mm above the coil. The magnetic field is measured behind shielding samples and $SE_H$ is calculated by:

$$\boldsymbol{SE_H = 20 \times \log_{10} \frac{H_{air}}{H_{shield}} = 20 \times \log_{10} \frac{B_{air}}{B_{shield}} = 20 \times \log_{10} \frac{V_{air}}{V_{shield}}} \quad \textbf{(1)}$$

Experimentally, $SE_H$ is calculated thanks to a Hall probe which its voltage V is proportional to the magnetic induction B. Sensitivity of the Hall probe was 5.0 ± 0.1 mV/G. $H_{shield}$ is the magnetic field above the sample at the measuring point while $H_{air}$ is at the same position without the sample. Measuring point is placed 5 mm above the sample.

[Figure 4 about here.]

A 3D-numerical model of magnetic shielding has been developed with AC/DC module of Comsol Multiphysics (version 5.2a). Due to symmetry, only a quarter sphere is modeled (Figure 4(b)). The simulated geometry is the experimental one: same size of coil, 3x3 $cm^2$ samples, coil-shield distance of 6 mm and coil-measuring point distance of 11 mm. The model domain is bounded by a thick layer of infinite elements. Magnetic shielding effectiveness $SE_H$ of initial Al and steel sheets and Al/Steel/Al composite with different reduction rates have been experimentally and numerically evaluated. In order to facilitate numerical calculation, a homogenization approach has been proposed to determine equivalent properties of Al/Steel/Al samples (Figure 5). The homogenization principle (Figure 5(a)) is to obtain the same shielding effectiveness of Al/Steel/Al multilayer with only one layer of a virtual material which has equivalent properties. Equivalent electrical conductivity and equivalent magnetic permeability are determined numerically by applying a potential difference at the bound of Al/Steel/Al composite (Figures 5(b,c)). The equivalent properties are deducted afterward from Joule losses ($J_L$) and magnetic energy ($W_{mag}$):

$$\boldsymbol{J_L = \frac{V_0^2}{R} = \int_{V_c} E \cdot J \, dV_c} \quad \textbf{(2)}$$

$$\boldsymbol{W_{mag} = \frac{1}{2} \Re \varphi^2 = \int_{V_c} \left( \int_0^B H \cdot dB \right) dV_c} \quad \textbf{(3)}$$

where $V_0$ = 1 V the electrical potential, $\varphi = A_0 \times c$, $A_0$ = 1 Wb/m the magnetic potential, c the width of sample, R the effective resistance and $\Re$ the effective reluctance. In Comsol Multiphysics, Joule losses and magnetic energy are calculated by integration over the total volume of the composite $V_c$ with E the electric field, J the current density, H the magnetic field and B the magnetic flux density. By applying potential difference at the different bounds, effective properties can be determined in each direction: rolling (RD), transverse (TD) and normal (ND) directions.

[Figure 5 about here.]

## 3. Results and discussions

### *3.1. Cold Roll Bonding (CRB)*

Plastic instability of steel has been observed during cold roll bonding of Al/Steel/Al sandwich. Figure 6 shows the surface aspect of the steel layer after dissolution of Al in a concentrated solution of NaOH for different reduction rate. A scanner is used with two different modes to scan these surfaces of 1x2 $cm^2$ sample. An opaque mode highlights the necking (Figures 6(a,b)) and a film mode highlights the fragmentation of the steel layer (Figure 6(c)) during CRB. The first 6 samples have been rolled with no lubricant. The evolution of necking and fragmentation in function of reduction rate can then be observed. For 48.3 %, necking is slightly visible and becomes more and more pronounced with the increase of the reduction rate until fragmentation. Fragmentation is reached from a reduction rate of 61.7 %, far from the theoretical one (13 %).

[Figure 6 about here.]

Higher fragmentation can be obtained with higher reduction. It is observed that the specimen laminated with lubricated rolls presents a more pronounced fragmentation. Due to the lubricant, the rolling is easier, the rolls are less repelled by the sample and then a higher reduction rate is obtained: 77.5 % with lubricated rolls, 75 % with non-lubricated rolls. It can also be noted that fragmentation is not uniform, some areas present higher fragmentation. Fragmentation rate has been quantified for 1x2 $cm^2$ samples presented in Figure 6(c) by:

$$\%\boldsymbol{Frag} = \frac{\boldsymbol{N_{wp}}}{\boldsymbol{N_{tp}}} \times \mathbf{100} \qquad \textbf{(4)}$$

[Figure 7 about here.]

with $N_{wp}$ the number of white pixels and $N_{tp}$ the total pixel number. The evolution of the fragmentation rate in function of reduction rate is presented in Figure 7. Before a reduction rate of 70 %, the fragmentation rate does not exceed 4 %. For 75 %, it reaches almost 14 % and exceeds 20 % for the last sample with lubricated rolls which is almost cut in half. This evolution is then quite exponential. Furthermore, during experiment, it has been observed that necking and fragmentation of the steel layer are sensible of CRB parameters. Then, small variations of parameters involve different fragmentation rate and explains the extent of error bars in Figure 7.

RD-ND cross-section of the first 5 samples have been polished and studied with optical microscopy (Figure 8(a)). Small thickness variations of steel layer are observed for 48.3 and 53.3 % that indicates the start of diffusion necking (red arrows). Local necking is observed for 61.7 and 65 %. Fragmentation of steel is observed for 69.2 %. Extruding and welding of the two Al layers are noted between fragmentation. From Figure 6 and Figure 8, necking and fragmentation show a certain periodicity which tends to decrease with the increase of reduction rate. RD-ND cross-sections obtained by the numerical approach are represented in Figure 8(b). Initial mesh is composed respectively of 20 µm and 10 µm mesh for Al layers and steel layer. Three numerical simulations are made for reduction rate of 50, 60 and 70 %. Periodical necking is reproduced successfully. For 50 %, a slight variation of steel thickness (≈ 1-2 µm), not visible to the naked eye, is remarked. Periodical necking is observed to be very similar in the case of a reduction rate of 60 %, with a spatial periodicity of about 450 µm. For 70 %, the results obtained with the numerical model are not relevant, as fragmentation modeling is complex due to mesh overlap. Moreover, steel thickness in experimental and numerical is really closed which its maximal value is around 50 µm. Periodical necking of a hard phase sandwiched between two soft phases has been studied numerically by Imai et al. [33] and Utsunomiya et al. [34] for theoretical elastic-perfectly plastic bodies. In their work, necking occurs for a reduction rate of 20 %. Materials properties influence have been highlighted, especially higher differences in yield stress facilitate necking occurrence. In our case, by considering materials behavior with a power law extrapolated from experimental tensile tests, the numerical model can determine accurately the onset of necking which is for a reduction rate around 50 %.

[Figure 8 about here.]

Plastic instability is a phenomenon amplified at higher rolling strains, but its origin is not totally understood, and no general criteria has been reported. However, Nowicke et al. [35], by approximating the stress state in rolling as a plane strain compression has theoretically shown that the harder phase is in tension along the rolling direction while the soft phase is in compression. The presence of tension in this direction explains necking formation. RD-ND cross-sections of simulated CRB are shown in Figure 9. Rolling and normal direction stress under rolls are represented for reduction rates of 50, 60 and 70 %. Along rolling direction, the following observations can be made:

[Figure 9 about here.]

- The steel layer is in tension principally at the entrance and weakly at the exit of rolls.
- Al layers are in compression under rolls.
- A rapid decrease in thickness of Al layers at the entrance could explain the tension of the steel layer which is dragged along by them.
- The tension at the exit could be explained by the compression stress relaxation in Al layers, since at this point Al/Steel interfaces are considered bonded.
- For higher reduction rate, the steel layer still goes through a compression zone where maximal compression in Al layers is observed. This result has not been predicted by Nowicke et al.

Along normal direction, the following remarks can be made:

- Steel and Al layers are in compression.
- A slightly larger compression is observed in steel.
- The compression in this direction promotes necking formation, and a higher compression for higher reduction rate could facilitate extrusion and welding of Al through steel fragmentation.

[Figure 10 about here.]

Stress at the surface of Al in contact with roll and in the center of steel layer along rolling axis are drawn in Figure 10. Length of contact between rolls and the strip increases with reduction rate.

Same observations than previously can be made. However, by drawing these curves, minimal value of stress following RD and ND can be observed at the same point (≈ -0.55 cm) from the exit for the three different reduction rates. This point is commonly named “neutral point” and represents the position where the speed of the strip surface is the same than the speed of rolls and where the shear stress changes direction [36]. Moreover, maximal value of the steel tension is attained at the entrance and is unexpectedly the same for different reduction rate. Necking occurrence cannot then be explained only by the tension of the steel layer. It is also observed that compression stress increases at the neutral point with reduction rate.

Necking occurrence can then be explained by tension of steel layer in rolling direction at the entrance, compression of steel and Al layers in normal direction but also by the thickness decrease at the entrance of Al and steel layers. Indeed, the tension at the entrance is the same for 50, 60 and 70 % reduction rate but as the thickness is lower for higher reduction, necking occurrence is easier. Moreover, the compression in normal direction of the steel layer facilitates necking and fragmentation emergence.

### *3.2. Tensile Bond Strength Test (TBST)*

To quantify adherence of the Al/Steel interface, TBST is performed. CRB of 1.5 cm width sample is carried out for different reduction rates. 1.5x1.5 cm$^2$ square samples are cut and glued between two Al bars. This assembly is put in a tubular furnace at 150 °C during 40 min. Tensile test is performed on about 8 samples for each reduction rate. Tensile Bond Strength (TBS) obtained for each reduction rate is presented in Figure 11. TBS increases quickly with reduction rate but shows great variations due to inhomogeneous necking and fragmentation and potential shear stress during TBST caused by misalignment of aluminum bars. For a reduction rate of 43.3 %, debonding can be attained during shot-peening, so TBST gives a low value around 0.1 MPa. Until about 58 %, TBS increases, and fracture occurs at the Al/Steel interface. Let us note that on average, the glue starts to weaken around 20 MPa in the present test conditions. So, for the two highest reduction rates, it is not the Al/Steel interface that breaks but mainly the glue which means the TBS of the Al/Steel interface is in fact greater that the reported points.

In Figure 12, several facies of Al layer after debonding are presented. For a reduction rate of 43.3 %, extrusion of Al is quasi non-existent. Extrusion is more and more pronounced with increase of reduction rate. For reduction rate greater than 63.3 %, the glue breaks before the Al/Steel interface which means that a good bond quality is attained, delamination or debonding of Al/Steel interfaces requires a complete deterioration of the composite. From these results, it can be concluded that necking and fragmentation of steel, that allows extrusion and welding of Al layers, are favorable to bond quality of Al/Steel/Al composite.

[Figure 11 about here.]

[Figure 12 about here.]

### *3.3. Magnetic Shielding*

Magnetic shielding of samples with different reduction rates is studied in near field at low frequency (1 Hz-10 kHz). A 3 cm diameter coil, alimented by a low frequency generator, generates a magnetic field. Magnetic induction is measured at 11 mm above the coil by a Hall probe of sensitivity of 5.0 ± 0.1 mV/G. Square samples of 3x3 cm$^2$ size are placed 6 mm above the coil. The system is put under airflow to limit temperature increase. For each sample, several measurements are made, and a reproducibility is observed. Figure 13 shows the experimental magnetic shielding effectiveness of these different samples. As expected, steel sheet (100 µm) shields at low frequency (~ 4.6 dB) due to its higher magnetic permeability. Al sheet (250 µm) starts to shield for frequencies around 500 Hz. $SE_H$ increases with frequency, this increase is more marked for Al sheet thanks to its higher electrical conductivity. Magnetic shielding of Al/Steel/Al tri-layer takes both behavior of steel and Al sheets: shielding at low frequency and pronounced increase towards high frequency. Shielding at low frequency is however lower than steel ones because steel thickness in the composite is lower than 100 µm. But at higher frequency, shielding of the composite can be better than steel and Al sheets. The impact of Al/Steel/Al thickness can be noticed. Higher reduction rate implies lower shielding. The impact of steel fragmentation on $SE_H$ is shown in Figure 14. The shielding decreases first linearly due to the decrease of thickness and continues to decrease with a steeper slope due to steel fragmentation. As a reminder, fragmentation of steel starts around 62 % and this point marked the beginning of slope change. It is observed that fragmentation has a more negative impact at 10 kHz than at 1 Hz. In a previous work, magnetic shielding of an Al/Steel composite produced by accumulative roll bonding (ARB) has been studied by Verstraete et al. [37] and it has been shown that fragmentation of steel is not as unfavorable to shielding as in the present study. In ARB, as steel layers are superimposed in this process, steel fragments are present on different levels through the composite thickness whereas in our case steel is present only in one plane inside the composite. This particular distribution in the case of ARB could explain that steel fragmentation is possibly not disadvantageous to magnetic shielding, or at least to a lesser extent.

[Figure 13 about here.]

[Figure 14 about here.]

Numerical simulation of magnetic shielding is realized with the same geometry and parameter than experimental one. For Al/Steel/Al sample, a homogenization method is used to facilitate 3D calculations. Equivalent properties are determined for the seven samples presented in Figure 6. A 3600x3600 pixels image equivalent to a 7.15x7.15 mm$^2$ image is considered as area for homogenization. Areas of fragmented specimen are presented in Figure 15. Total thickness is measured with a micrometer and layers thickness is determined by:

$$\boldsymbol{t_{steel} = \frac{t_{total} \times R_{vol}}{1 - \tau_{frag}}} \qquad \textbf{(5)}$$

$$\boldsymbol{t_{Al} = \frac{t_{total} - t_{steel}}{2}} \qquad \textbf{(6)}$$

with $t_{total}$, $t_{steel,}$ $t_{Al}$ respectively the total, steel and Al layers thickness, $R_{vol}$ the volume ratio and $\tau_{frag}$ the fragmentation rate of steel layer. It has been experimentally observed that volume ratio does not change with reduction rate. Initial volume ratio of 1/6 is then kept for numerical simulation. A parallelepiped of dimensions 7,15x7,15 mm$^2$ composed of the three layers (Al/Steel/Al) can then be modelized. For fragmented specimen, material properties of the modelized steel layer are defined by using images presented in Figure 15 extrapolated over all its thickness (Figure 16):

$$\boldsymbol{\sigma_{mat} = \sigma_{steel} + (\sigma_{Al} - \sigma_{steel}) \times im(x,y)} \quad \textbf{(7)}$$

$$\boldsymbol{\mu_{mat} = \mu_{steel} + (\mu_{Al} - \mu_{steel}) \times im(x,y)} \quad \textbf{(8)}$$

[Figure 15 about here.]

[Figure 16 about here.]

with $\sigma$ the electrical conductivity, $\mu$ the magnetic permeability and im(x,y) an indicator function defined from images where im(x,y) = 0 for black pixel and im(x,y) = 1 for white pixel.

In order to modelize accurately magnetic shielding, electrical conductivity and magnetic permeability of Al and steel sheets have to be determined. Electrical conductivity is first calculated from electrical resistivity measured by 4-point probes method. An averaging of 10 measures is considered. Al and steel sheets have respectively an electrical conductivity of $33.61 \times 10^6$ and $9.02 \times 10^6$ S/m. No experimental method to measure magnetic permeability of a thin sheet is available. So, magnetic permeability of steel is determined numerically. Low frequency magnetic shielding effectiveness of steel depends only of its magnetic permeability. Numerical results are then reconciled with experimental results by varying permeability in 4 cases: 3x3 cm$^2$ sample with 11 mm coil-probe distance, 10x10 cm$^2$ sample with 11, 16 and 24 mm coil-probe distance. Optimal value found by this method is a relative magnetic permeability $\mu_{steel}$ of 250 (typical relative permeability of a low carbon steel is between 100 and 1000). Evolution of equivalent properties determined by numerical homogenization is represented in Figure 17 in function of reduction and fragmentation rates. Magnetic permeability is really influenced by fragmentation of steel (Figure 17 (a,c)), especially in rolling direction (RD). The magnetic flux is mainly concentrated in steel and tries to avoid the steel fragmentation that are full of aluminum. Due to the geometry of fragmentation, the circumvention is easier following TD than RD and explains the stronger influence in RD. On the contrary, conductivity is almost not influenced, a very little decrease is observed (Figure 17 (b,d)). Electrical flux is mainly in Al layers and then is not much influenced by fragmentation. Electrical conductivity of Al/Steel/Al obtained by homogenization is around $29.3\text{-}29.5 \times 10^6$ S/m and tends to decrease slightly with thickness. Measure of 4-point probes method on Al/Steel/Al gives an electrical conductivity of 28.4 and 29.8 × 10$^6$ S/m for respectively 270 and 185 µm thickness samples. Numerical homogenization gives then accurately electrical conductivity of Al/Steel/Al tri-layer composites. The slight difference for the 270 µm composite could be explained by presence of small gaps at the Al/Steel interfaces, which increase electrical resistivity measured by 4-point probes method.

[Figure 17 about here.]

[Figure 18 about here.]

[Figure 19 about here.]

Steel and Al properties are implemented in numerical simulation. Figure 18 and 19 shows respectively the numerical magnetic shielding effectiveness of these different samples and the numerical impact of steel fragmentation. Observations proposed for the experimental results are still valid for numerical ones. Steel layer shields at low frequency (~ 4.7 dB), Al sheet starts to shield at around 500 Hz, but the increase is faster, and Al/Steel/Al composites take both behaviors. Steel fragmentation has also a negative impact on magnetic shielding in numerical simulation, but its impact is similar at 1 Hz and 10 kHz. Thickness decrease and steel fragmentation have the same impact at low frequency in experimental and numerical models, slopes of straight line are very similar. However, at high frequency, they have a more pronounced influence in numerical model, slopes of straight line are bigger. A more detailed comparison between experimental and numerical model results is presented in Figure 20. A good correlation is obtained at low frequency (<1 kHz) on each sample. Magnetic shielding of steel layer is accurately reproduced for all frequencies (1 Hz – 10 kHz). However, magnetic shielding of Al layer is higher in numerical model for high frequency (> 5 kHz), and then this gap is also observed for the composite. At 10 kHz, the difference is around 1.4 dB for Al, 4.8 dB for composite at 53.3 % and 2.3 dB for composite at 69.2 %.

[Figure 20 about here.]

In order to explain this difference, several parameters have been investigated:

- First, the proposed numerical model is only based on an electromagnetic formulation and the impact of temperature was not initially considered. Actually, the coil tends to heat the system due to Joule effect. This heat will influence the Hall probe measurements (±0.02%/°C for null shift and ±0.02%/°C in sensitivity). Furthermore, Eddy currents in Al layer tend also to heat the sample. Temperature increase of Al layer decreases its electrical conductivity (Eq. 9), and then decreases its shielding effectiveness.

  $$\boldsymbol{\sigma_{Al} = \frac{\sigma_0}{1+\alpha\Delta T}} \qquad \textbf{(9)}$$

  with $\sigma_0$ the electrical conductivity of Al at room temperature, $\Delta T$ the temperature difference and $\alpha$ the temperature coefficient equal to $4 \times 10^{-3}$ $K^{-1}$ for Al. With the use of airflow, the observed experimental temperature increase is between 5-10 °C. Considering the corresponding impact on the electrical conductivity, a decrease of 0.14-0.28 dB is obtained at 10 kHz with the numerical model for Al shielding.

- The difference between experimental/numerical results is higher for composite cases. In general, the electrical conductivity is considered to be decreased by cold working due to introduction of defects. However, 4-point probe measures and numerical homogenization of composite give very close values of conductivity. The difference is also higher for lower reduction rate. It could be explained by the fact that perfect Al/Steel interface is considered in numerical model and that steel necking is not taken into account. Nevertheless, it is still a challenge to quantify this impact. However, considering the impact of temperature, a decrease of 0.21-0.41 dB and 0.14-0.28 dB is obtained at 10 kHz with the numerical model for respectively 310 µm (53.3 %) and 185 µm (69.2 %) composites. The impact of temperature is then higher for thicker sample.

- Moreover, experimental sample flatness is not perfect, especially for composite, and could reduce $SE_H$. A decrease of around 0.1 dB has been observed by bending slightly the sample in the numerical model.

- Finally, the impact of mesh size in the numerical model has been studied but the influence has shown to be negligible.

## 4. Conclusion

For the purpose of magnetic shielding, Al/Steel/Al sandwich is produced by cold roll bonding at different reduction rates. Its composition and design make it a good candidate to shield devices from low frequency magnetic fields. The composite structure, dependent on reduction rates, influences adherence of Al/Steel interfaces and shielding effectiveness. The following observations are done:

- Necking of steel starts for a reduction rate around 50 % and evolves until fragmentation at around 62 %. The size of fragmented zones increases with reduction rate. Fragmentation rate attains 20 % for a reduction rate of 77.5 %.

- Steel necking is successfully reproduced in numerical model, although steel fragmentation cannot be modelized. Necking occurrence can be explained by tensile stress of steel layer following RD, compression stress following ND and decrease of Al and steel layers thickness at the rolls entrance.

- A better bond quality is obtained with increase of reduction rate and then with increase of extruded Al into steel necking. Moreover, for the highest reduction rate (around 67 %), Tensile Bond Strength can reach up to 50 MPa.

- Steel layer shields over the entire frequency range (1 Hz – 10 kHz) while Al layer starts to shield around 500 Hz, but its growth is more pronounced. The sandwich composite proposes an interesting compromise of both behaviors. However, steel fragmentation has a negative impact on shielding effectiveness and tends to get worse at higher frequency.

- Electrical conductivities measured by 4-point probe method and that obtained by homogenization are similar. Numerical model and experimental results are in good correlation for the steel layer over the studied frequency range, and at low frequency (< 1 kHz) for Al layer and composites. For the latter, a discrepancy is observed for frequencies higher than 5 kHz and several parameters that influence shielding effectiveness has been proposed, especially temperature increase seen in experimental.

Therefore, thickness reduction and steel fragmentation have a negative effect on SE but for optimal mechanical properties, composite must have a good adherence of Al/Steel interfaces. Then optimal condition between SE and mechanical strength is obtained around 62 % reduction rate where only few fragmentations are observed, and Al/Steel interfaces have a tensile bond strength of 20 MPa minimum.

## Acknowledgments

This work is supported by a public grant overseen by the French National Research Agency (ANR) as part of the “Investissement d’Avenir” program, through the “IDI 2016” project funded by the IDEX Paris-Saclay, ANR-11-IDEX-0003-02.

Authors would like to thank Eurofoil for the supply of aluminum sheets and Aurore Brézard-Oudot (GeePs) for the 4-point probe resistivity measurements.

## References

[1] R. Smolenski, J. Bojarski, A. Kempski, P. Lezynski, Time-domain-based assessment of data transmission error probability in smart grids with electromagnetic interference, IEEE Trans. Ind. Electron 61 (2014) 1882–1890.

[2] T. W. Dawson, K. Caputa, M. A. Stuchly, R. B. Shepard, R. Kavet, A. Sastre, Pacemaker interference by magnetic fields at power line frequencies, IEEE Trans. Biomed. Eng 49 (2002) 254–262.

[3] M. Carlberg, T. Koppel, M. Ahonen, L. Hardell, Case-Control study on occupational exposure to extremely low-frequency electromagnetic fields and the association with meningioma, BioMed Res. Int. 2018 (2018) 1-6
URL 10.1155/2018/5912394

[4] T. Koppel, I. Vilcane, P. Tint, Risk management of magnetic field from industrial induction heater–a case study, 16th international scientific conference engineering for rural development, Latvia University of Agriculture (2017)
URL 10.22616/ERDev2017.16.N218

[5] X. Liu, J. Wu, J. He, L. Zhang, Electromagnetic interference shielding effectiveness of titanium carbide sheets, Materials Letters 205 (2017) 261–263.
URL 10.1016/j.matlet.2017.06.101

[6] Z. Xu, H. Hao, Electromagnetic interference shielding effectiveness of aluminum foams with different porosity, Journal of Alloys and Compounds 617 (2014) 207–213.
URL 10.1016/j.jallcom.2014.07.188

[7] D. D. L. Chung, Electromagnetic interference shielding effectiveness of carbon materials, Carbon 39 (2) (2001) 279–285.
URL 10.1016/S0008-6223(00)00184-6

[8] M. Z. Li, L. C. Jia, X. P. Zhang, D. X. Yan, Q. C. Zhang, Z. M. Li, Robust carbon nanotube foam for efficient electromagnetic interference shielding and microwave absorption, Journal of Colloid and Interface Science 530 (2018) 113–119.
URL 10.1016/j.jcis.2018.06.052

[9] A. A. Al-Ghamdi, O. A. Al-Hartomy, F. El-Tantalwy, F. Yakuphanoglu, Novel polyvinyl alcohol/silver hybrid nanocomposites for high performance electromagnetic wave shielding effectiveness, Microsyst Technol 21 (4) (2015) 859–868.

[10] M. Ray, J. J. George, A. Chakraborty, A. K. Bhowmick, An investigation of the electromagnetic shielding effectiveness of ethylene vinyl acetate elastomer reinforced with carbon nanofillers, Polym Polym Compos 18 (2010) 59-65

[11] Z. Dou, G. Wu, X. Huang, D. Sun, L. Jiang, Electromagnetic shielding effectiveness of aluminum alloy–fly ash composites, Compos Appl Sci Manuf 38 (1) (2007) 186–191.

[12] J. Ling, W. Zhai, W. Feng, B. Shen, J. Zhang, W. Zheng, Facile preparation of light-weight microcellular polyetherimide/graphene composite foams for electromagnetic interference shielding, ACS Appl Mater Interfaces 5 (7) (2013) 2677-2684

[13] X. Ma, Q. Zhang, Z. Luo, X. Lin, G. Wu, A novel structure of Ferro-Aluminum based sandwich

composite for magnetic and electromagnetic interference shielding, Materials and Design 89 (2016) 71–77.
URL 10.1016/j.matdes.2015.09.137

[14] D. H. Kim, Y. Kim, J. W. Kim, Transparent and flexible film for shielding electromagnetic interference, Materials and Design 89 (2016) 703–707.
URL 10.1016/j.matdes.2015.09.142

[15] Schelkunoff, S.A., Electromagnetic Waves, Bell Telephone Laboratories series (1943), Van Nostrand

[16] L. Prévond, N. Collard, R. Caplain, P. François, Method for manufacturing a metal assembly (2016), US patent, US9382610B2

[17] W. Abdelli, X. Mininger, L. Pichon, H. Trabelsi, Impact of composite materials on the shielding effectiveness of enclosures, Applied Computational Electromagnetics Society Journal 27 (4) (2012) 369–375.

[18] I. K. Kim, S. I. Hong, Mechanochemical joining in cold roll-cladding of tri-layered Cu/Al/Cu composite and the interface cracking behavior, Materials and Design 57 (2014) 625–631.
URL 10.1016/j.matdes.2014.01.054

[19] R. Jamaati, M. R. Toroghinejad, Investigation of the parameters of the cold roll bonding (CRB) process, Materials Science and Engineering A 527 (9) (2010) 2320–2326.
URL 10.1016/j.msea.2009.11.069

[20] M. Eizadjou, H. D. Manesh, K. Janghorban, Investigation of roll bonding between aluminum alloy strips, Materials and Design 29 (4) (2008) 909–913.
URL 10.1016/j.matdes.2007.03.020

[21] L. Li, K. Nagai, F. Yin, Progress in cold roll bonding of metals, Science and Technology of Advanced Materials 9 (2) (2008) 023001
URL 10.1088/1468-6996/9/2/023001

[22] M. Hosseini, H. D. Manesh, Bond strength optimization of Ti/Cu/Ti clad composites produced by roll-bonding, Materials and Design 81 (2015) 122–132.

[23] M. Naseri, M. Reihanian, E. Borhani, Bonding behavior during cold roll-cladding of tri-layered Al/brass/Al composite, Journal of Manufacturing Processes 24 (2016) 125–137.
URL 10.1016/j.jmapro.2016.08.008

[24] R. Abedi, A. Akbarzadeh, Bond strength and mechanical properties of three-layered St/AZ31/St composite fabricated by roll bonding, Materials and Design 88 (2015) 880–888.
URL 10.1016/j.matdes.2015.09.043

[25] R. Jamaati, M. R. Toroghinejad, Effect of friction, annealing conditions and hardness on the bond strength of Al/Al strips produced by cold roll bonding process, Materials and Design 31 (9) (2010) 4508–4513.
URL 10.1016/j.matdes.2010.04.022

[26] H. Manesh, H. Shahabi, Effective parameters on bonding strength of roll bonded Al/St/Al multilayer strips, Journal of Alloys and Compounds (2009) 292–299.
URL 10.1016/j.jallcom.2008.08.081

[27] C. Gao, L. Li, X. Chen, D. Zhou, C. Tang, The effect of surface preparation on the bond strength of Al-St strips in CRB process, Materials and Design 107 (2016) 205–211.
URL 10.1016/j.matdes.2016.05.112

[28] V. Y. Mehr, M. R. Toroghinejad, A. Rezaeian, The effects of oxide film and annealing treatment on the bond strength of Al-Cu strips in cold roll bonding process, Materials and Design 53 (January) (2014) 174–181.
URL 10.1016/j.matdes.2013.06.028

[29] H. D. Manesh, A. K. Taheri, Bond strength and formability of an aluminum-clad steel sheet, Journal of Alloys and Compounds 361 (1-2) (2003) 138–143.
URL 10.1016/S0925-8388(03)00392-X

[30] M. Talebian, M. Alizadeh, Manufacturing Al/steel multilayered composite by accumulative roll bonding and the effects of subsequent annealing on the microstructural and mechanical characteristics, Material Science and Engineering A 590 (2014) 186–193.
URL 10.1016/j.msea.2013.10.026

[31] Y. M. Hwang, H. H. Hsu, H. J. Lee, Analysis of plastic instability during sandwich sheet rolling, International Journal of Machine Tools and Manufacture 36 (1) (1996) 47–62.

URL 10.1016/0890-6955(95)92628-C

[32] M. Reihanian, M. Naseri, An analytical approach for necking and fracture of hard layer during accumulative roll bonding (ARB) of metallic multilayer, Materials and Design 89 (2016) 1213–1222.
URL 10.1016/j.matdes.2015.10.088

[33] T. Imai, H. Utsunomiya, R. Matsumoto, Finite Element Analysis of Plastic Instability Phenomenon in Cold Rolling of Clad Sheets, Procedia Engineering 184 (2017) 306–312.
URL 10.1016/j.proeng.2017.04.099

[34] H. Utsunomiya, S. Maeda, T. Imai, R. Matsumoto, Necking condition of layers in clad sheets during rolling, CIRP Annals 67 (1) (2018) 317–320.
URL 10.1016/j.cirp.2018.04.056

[35] F. Nowicke, A. Zavaliangos, H. C. Rogers, The effect of roll and clad sheet geometry on the necking instability during rolling of clad sheet metals, International Journal of Mechanical Sciences 48 (8) (2006) 868–877.
URL 10.1016/j.ijmecsci.2006.01.021

[36] C. J. Cawthorn, J. J. Minton, E. J. Brambley, Asymptotic analysis of cold sandwich rolling, International Journal of Mechanical Sciences 106 (2016) 184–193.
URL 10.1016/j.ijmecsci.2015.12.012

[37] K. Verstraete, L. Prévond, A.-L. Herbert, T. Baudin, Magnetic shielding at low frequencies: application for an aluminum/steel composite elaborated by Accumulative Roll Bonding, Advanced Engineering Materials (2019)
URL 10.1002/adem.201800967

## List of Figures

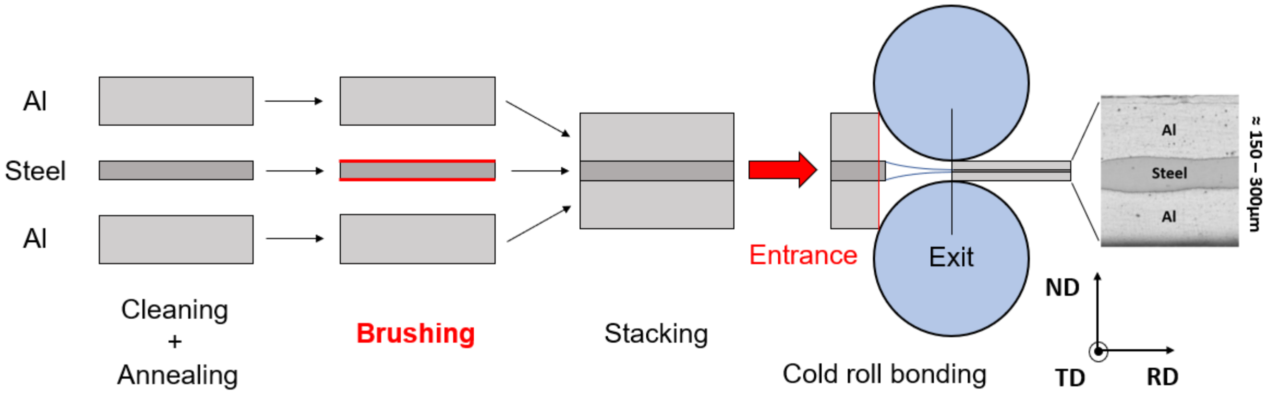

Figure 1: Cold roll bonding process of Al/Steel/Al composite

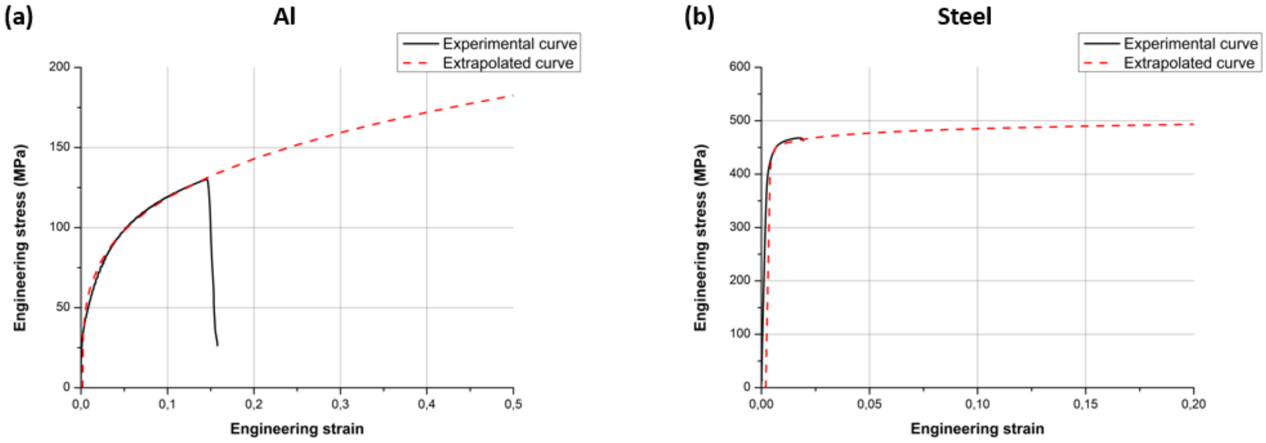

Figure 2: Extrapolated materials behavior, Al (a) and steel (b) sheets

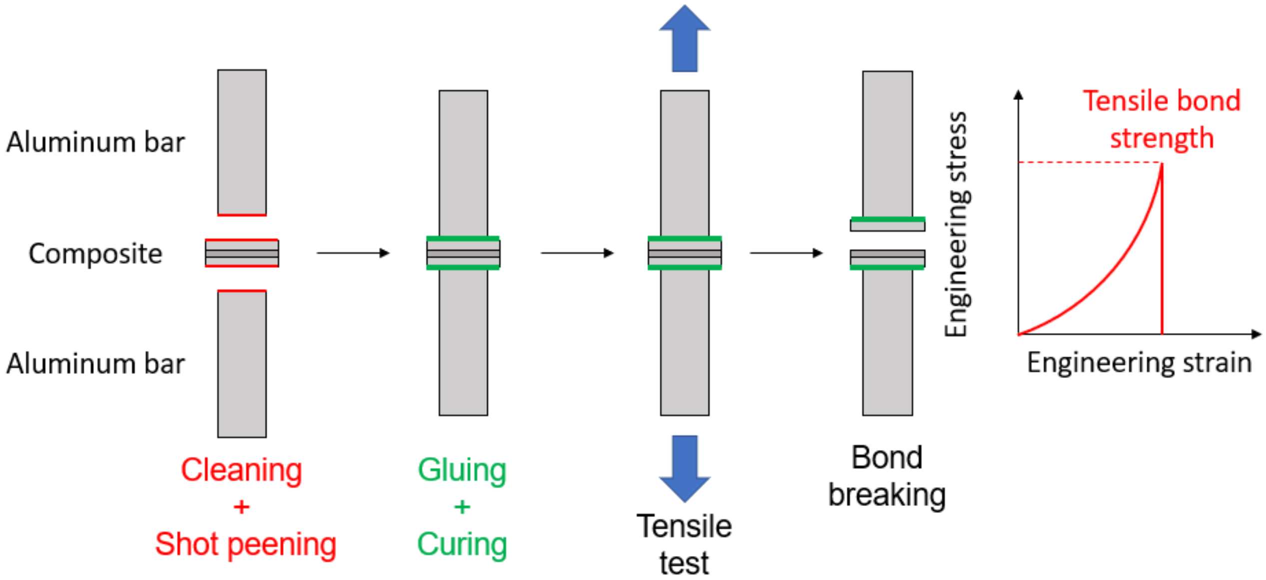

Figure 3: Tensile Bond Strength Test (TBST)

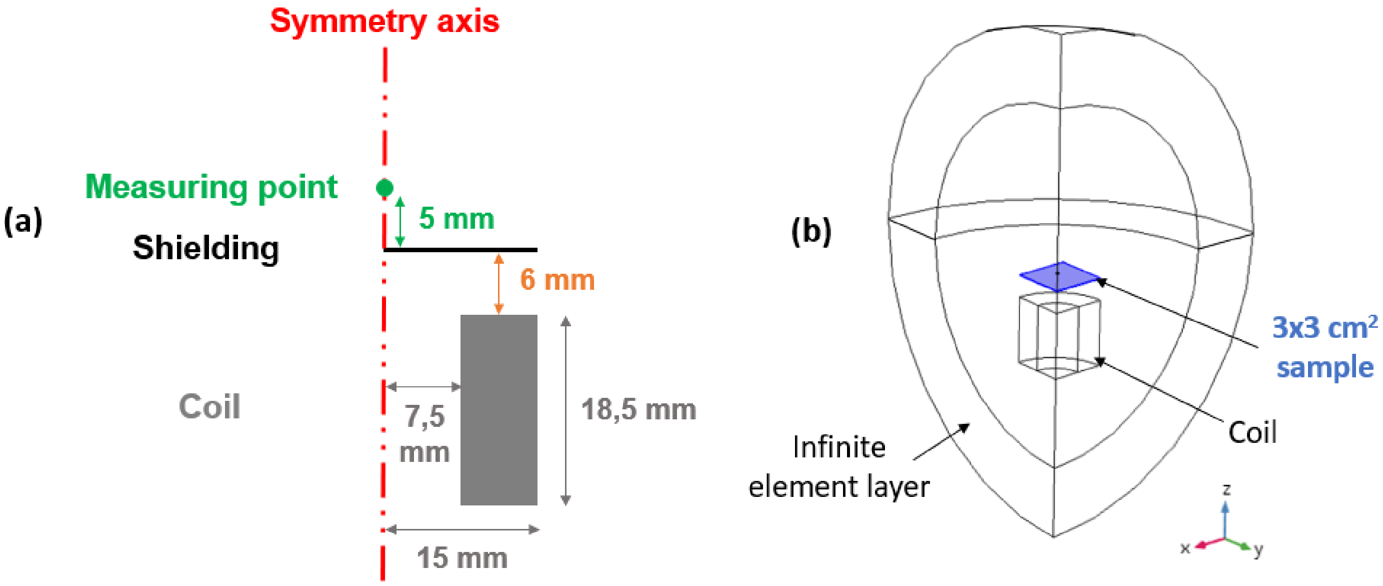

Figure 4: 2D schema (a) and 3D model (b) of magnetic shielding

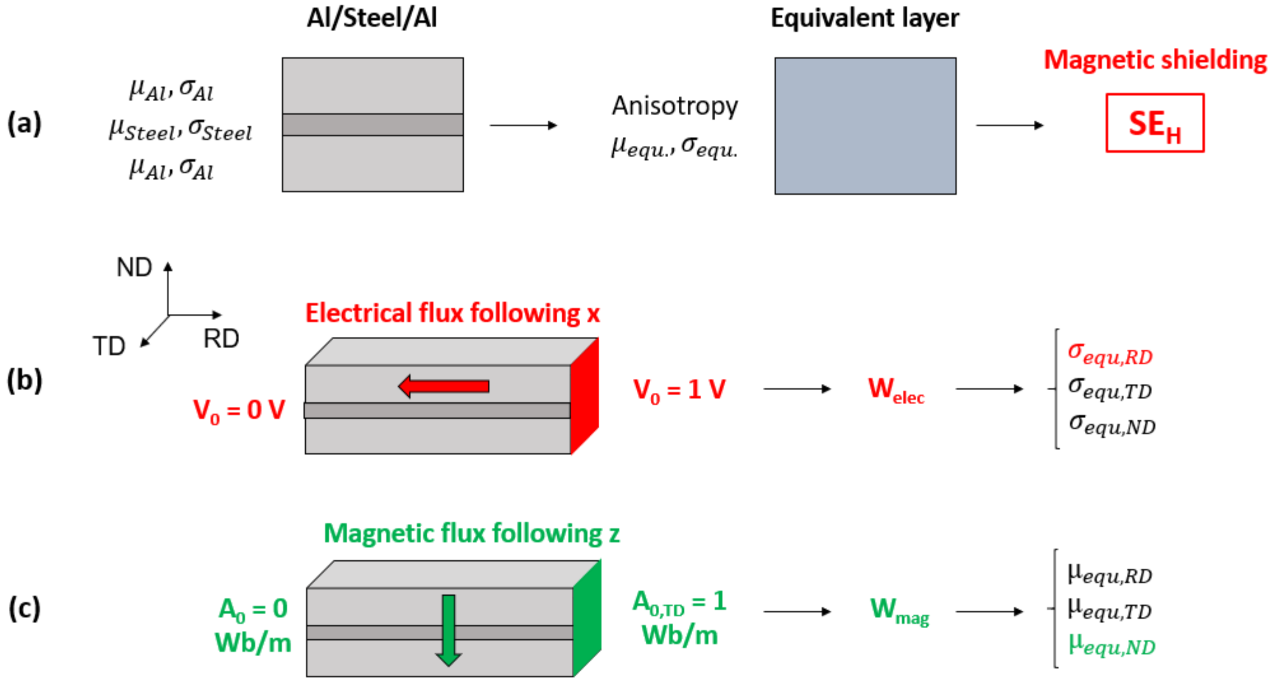

Figure 5: Homogenization of the tri-layer composite, principle (a) and calculation of equivalent electrical conductivity (b) and equivalent magnetic permeability (c)

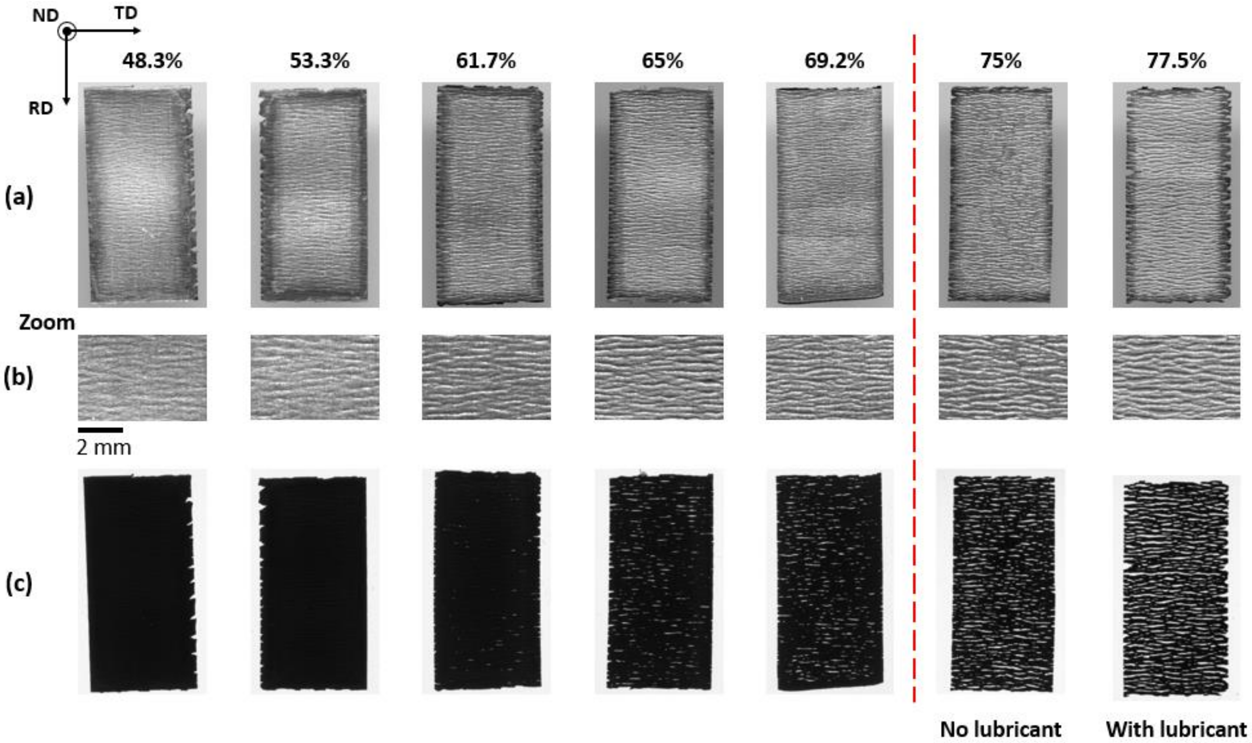

Figure 6: Necking and fragmentation of steel during CRB for different reduction rates, opaque scan (a, b), film scan (c)

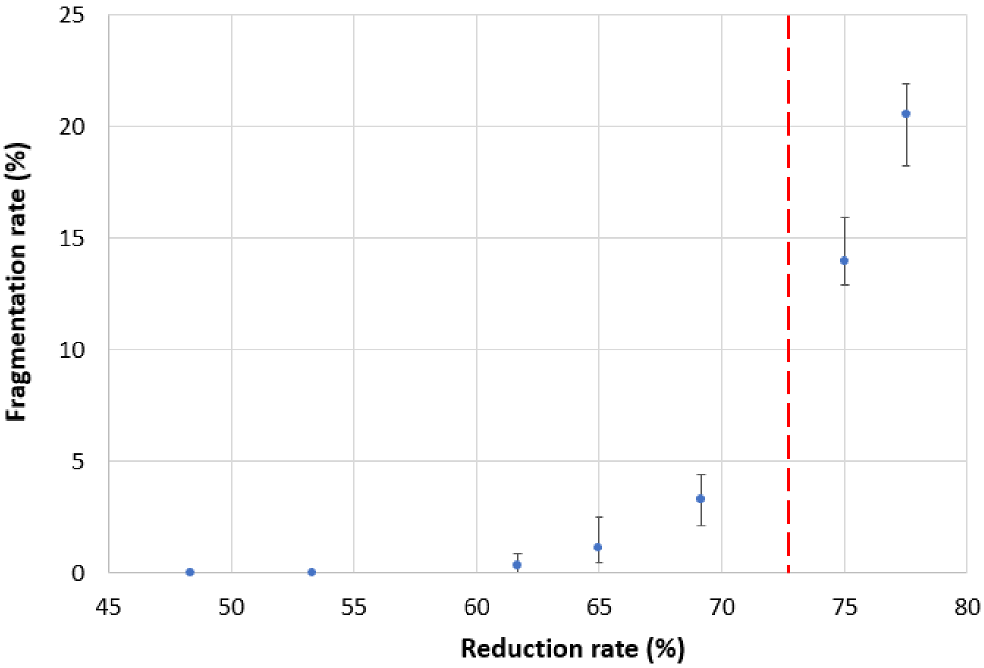

Figure 7: Fragmentation rate in function of reduction rate for 1x2 cm² samples

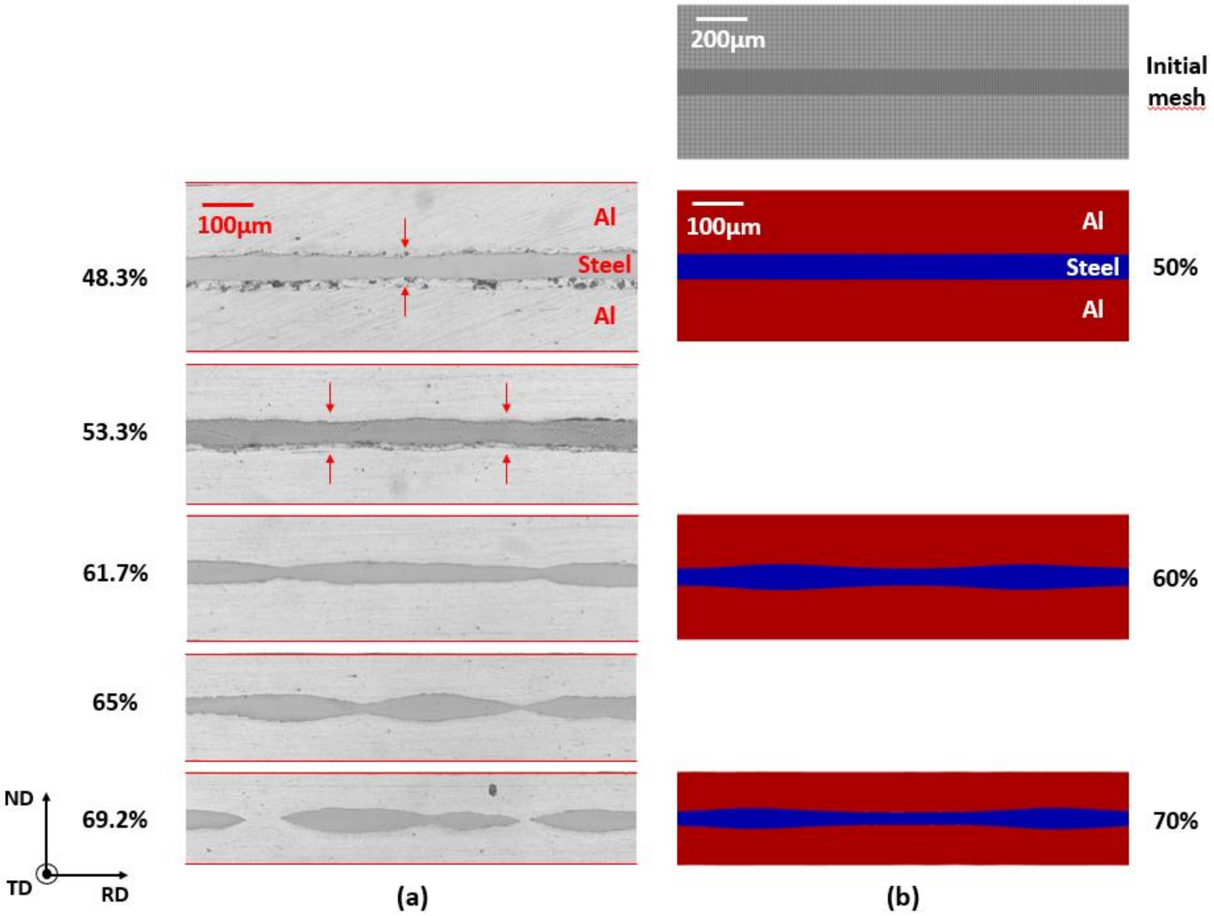

Figure 8: RD-ND cross-section of samples for different reduction rates, experimental (a), numerical (b)

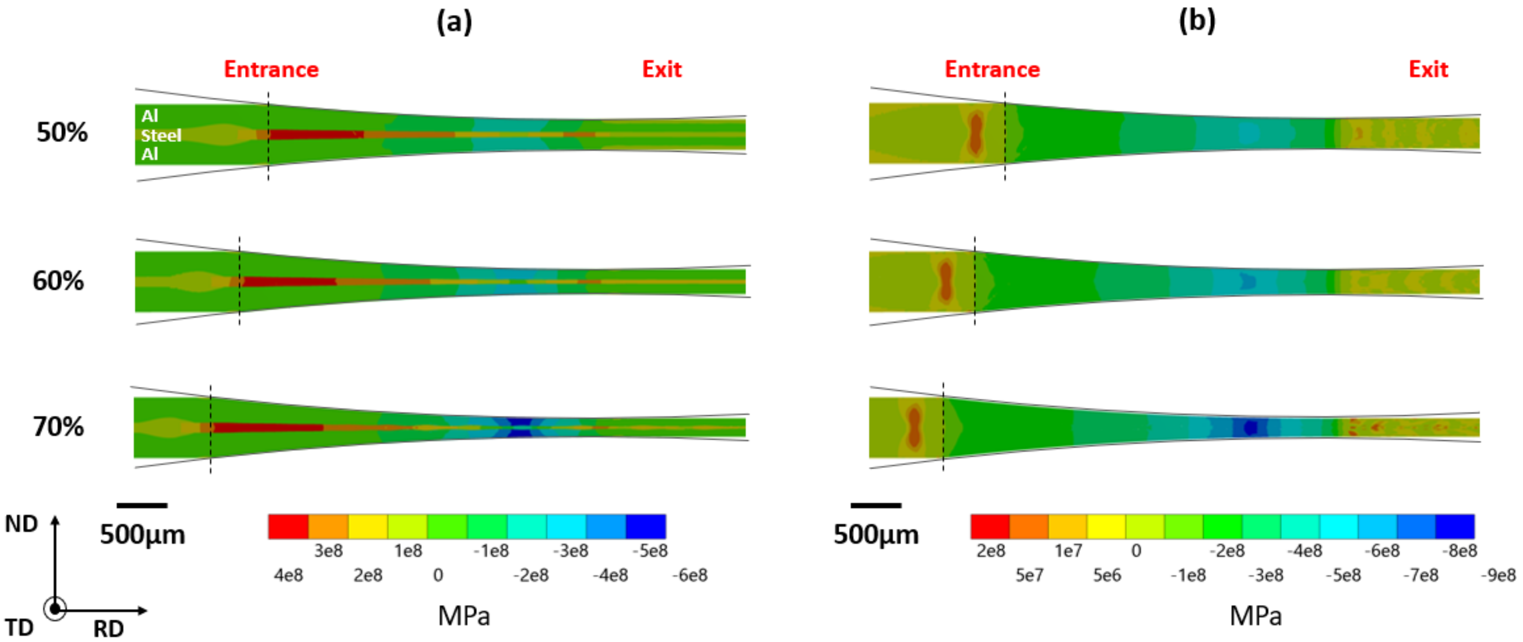

Figure 9: RD-ND cross-section of simulated CRB, rolling (a) and normal (b) direction stresses

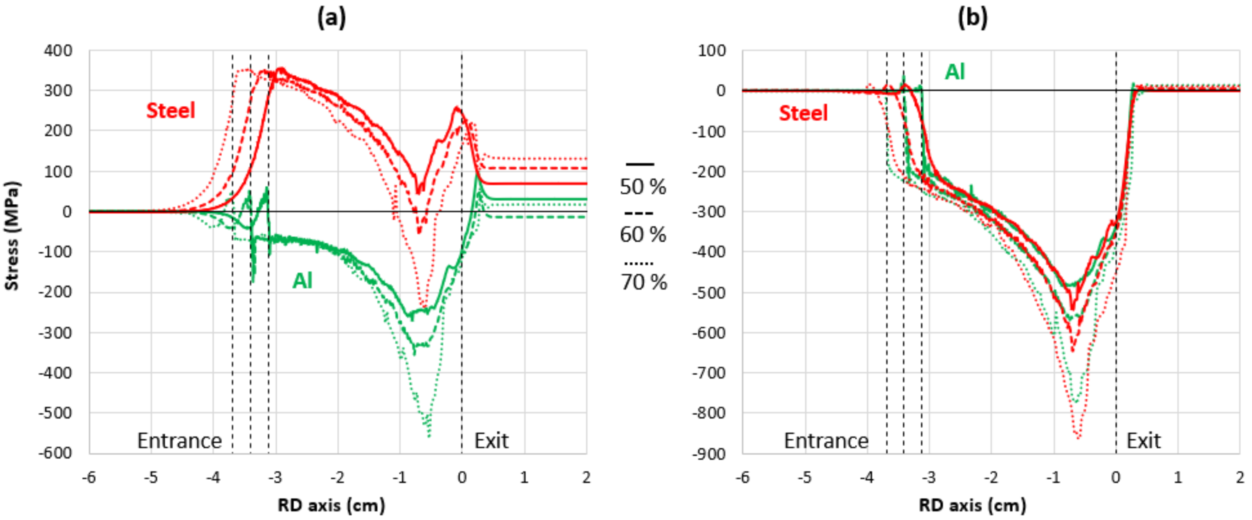

Figure 10: Numerical rolling (a) and normal (b) direction stress in center of steel and in surface of Al

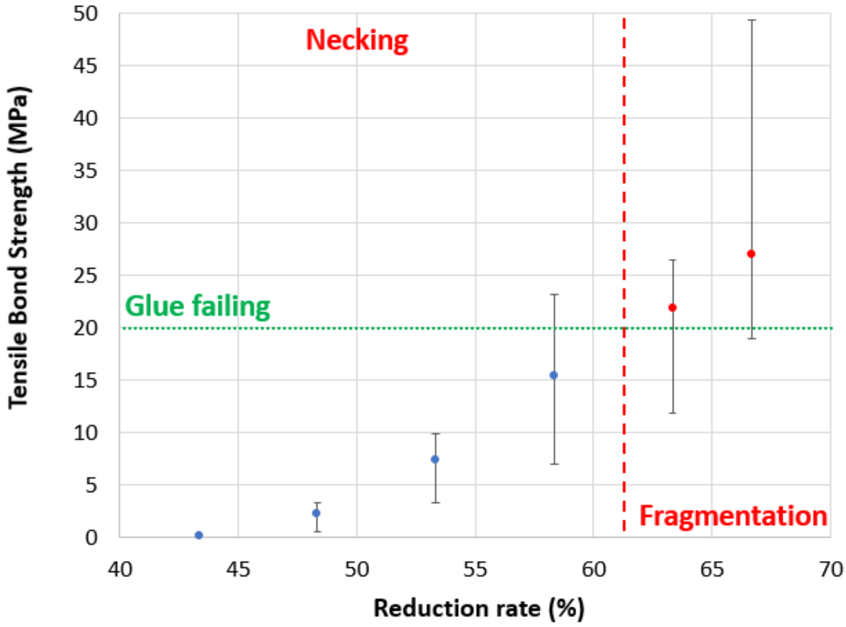

Figure 11: Tensile Bond Strength (TBS) of 1.5x1.5 cm² sample in function of reduction rate

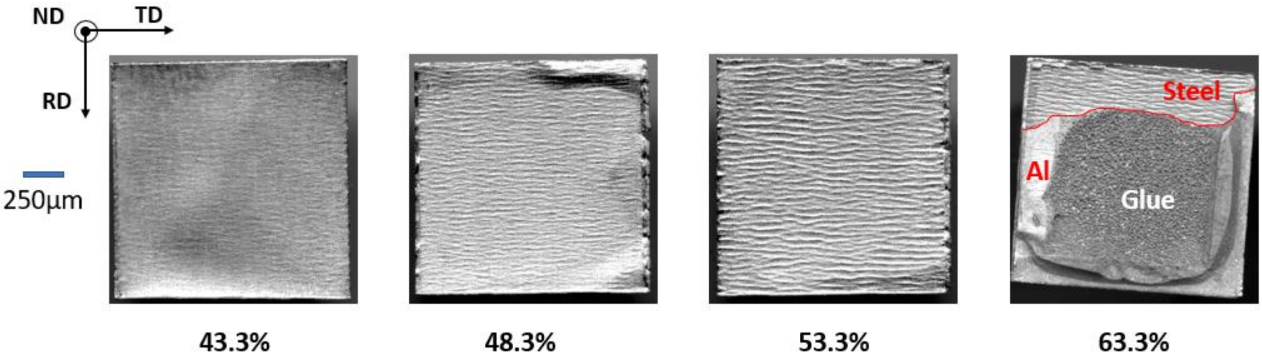

Figure 12: Facies of Al (1.5x1.5 cm²) after debonding in TBST in function of several reduction rate

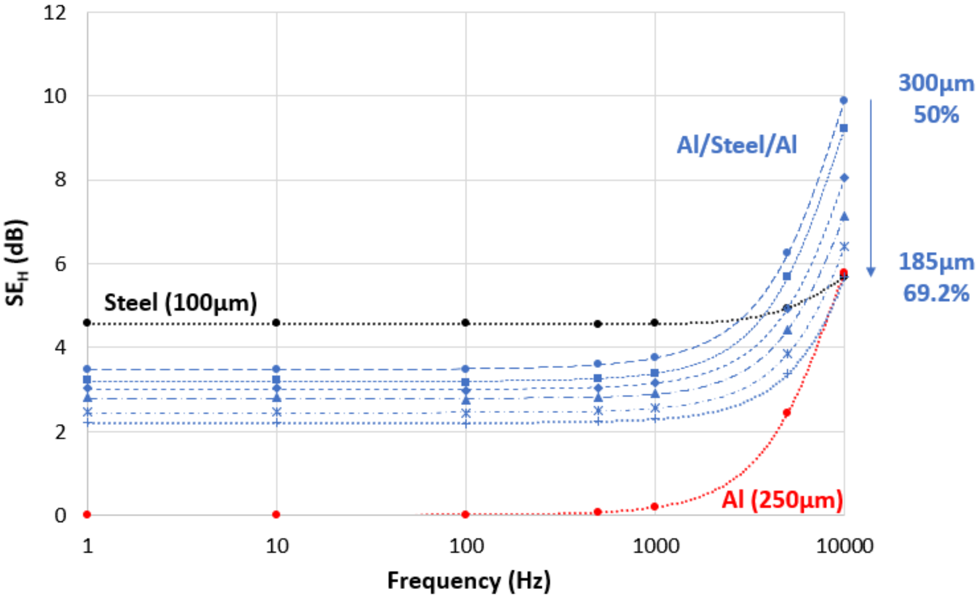

Figure 13: Experimental magnetic shielding effectiveness of 3x3 cm² samples

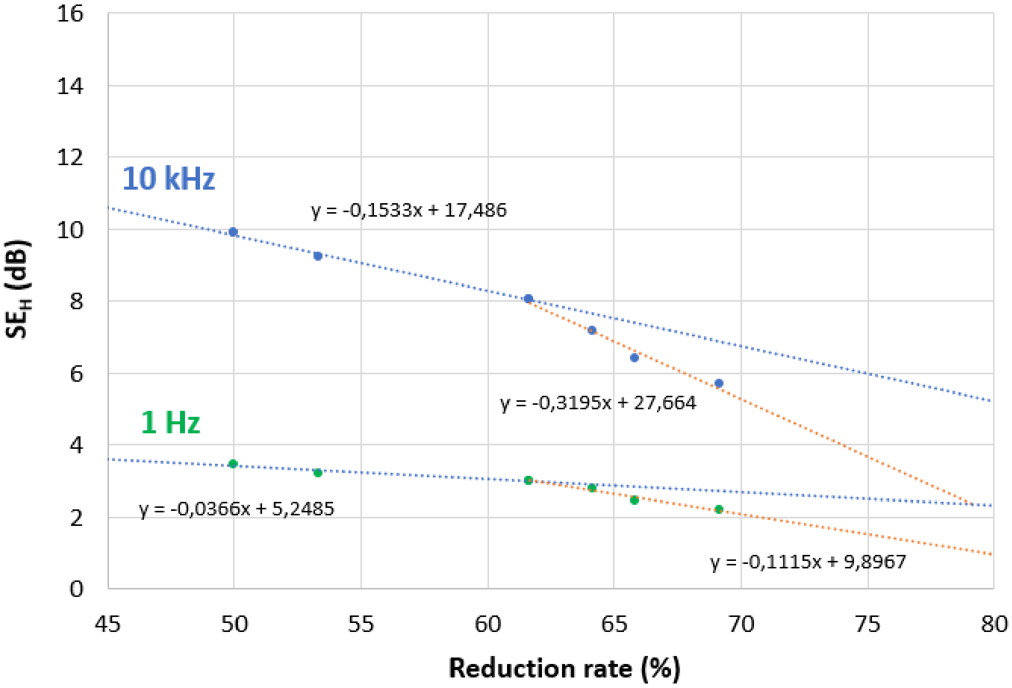

Figure 14: Experimental impact of fragmentation on $SE_H$ for 1 Hz and 10 kHz

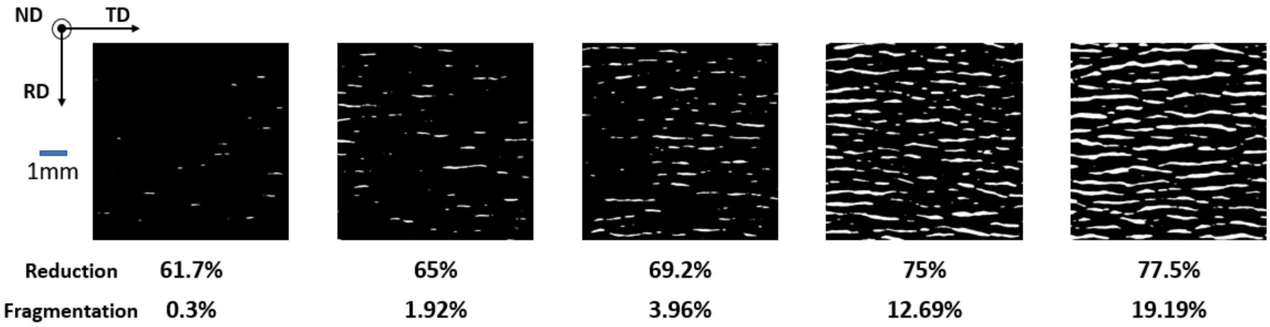

Figure 15: Fragmented specimen (steel) used in magnetic shielding model

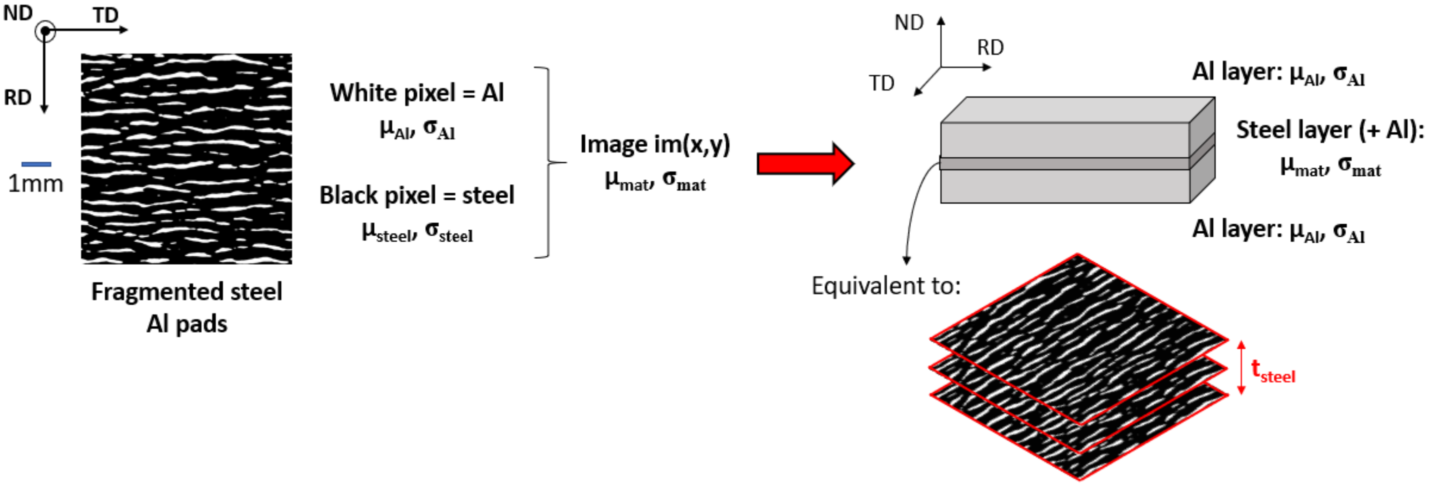

Figure 16: Consideration of steel fragmentation in magnetic shielding model

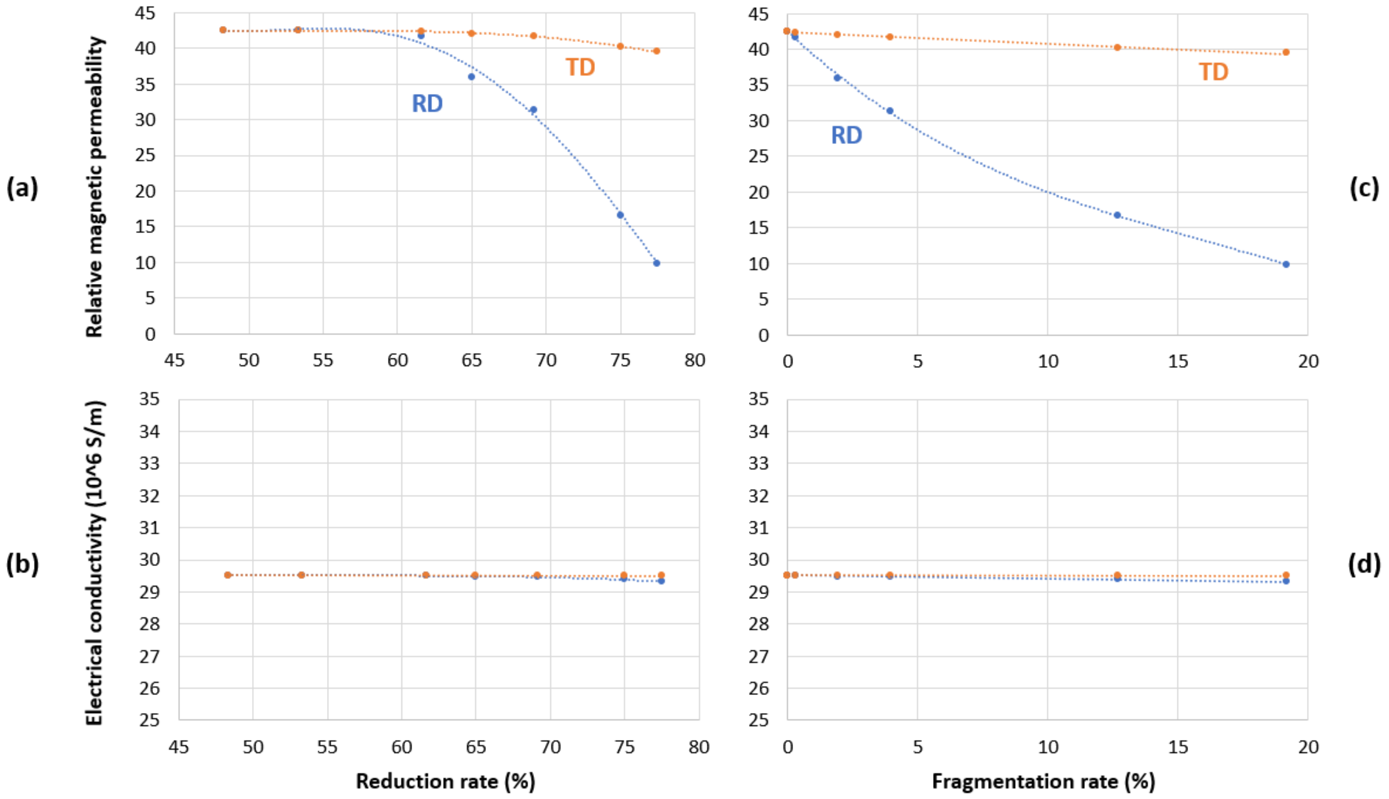

Figure 17: Equivalent properties following RD and TD in function of reduction (a,b) and fragmentation (c,d) rates, relative magnetic permeability (a,c) and electrical conductivity (b,d)

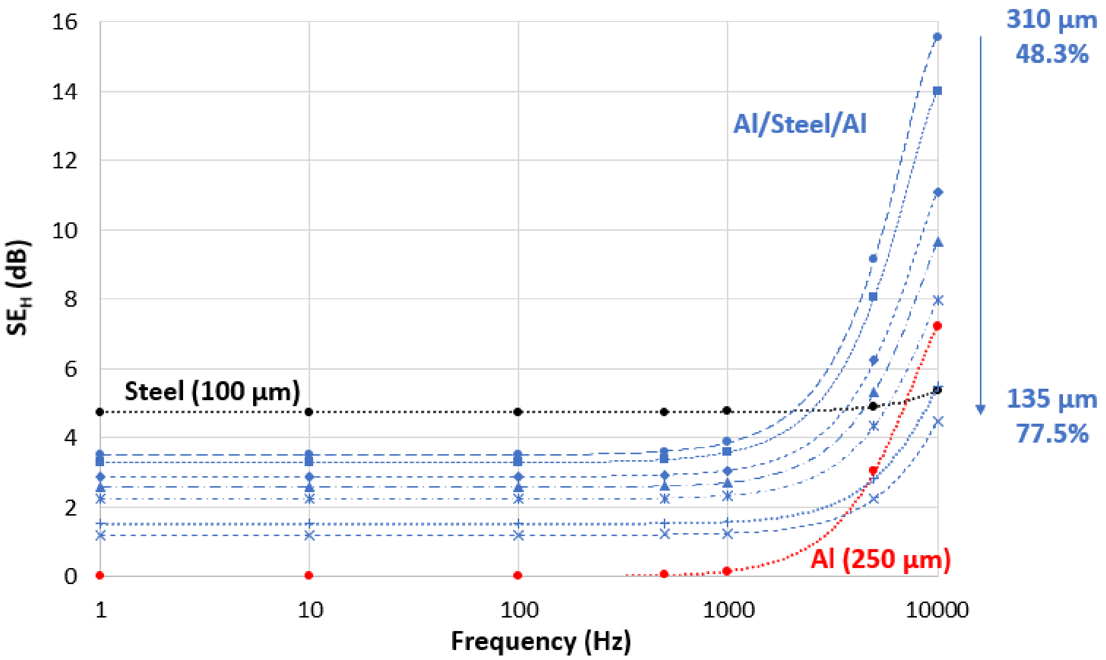

Figure 18: Numerical magnetic shielding effectiveness of 3x3 cm² samples

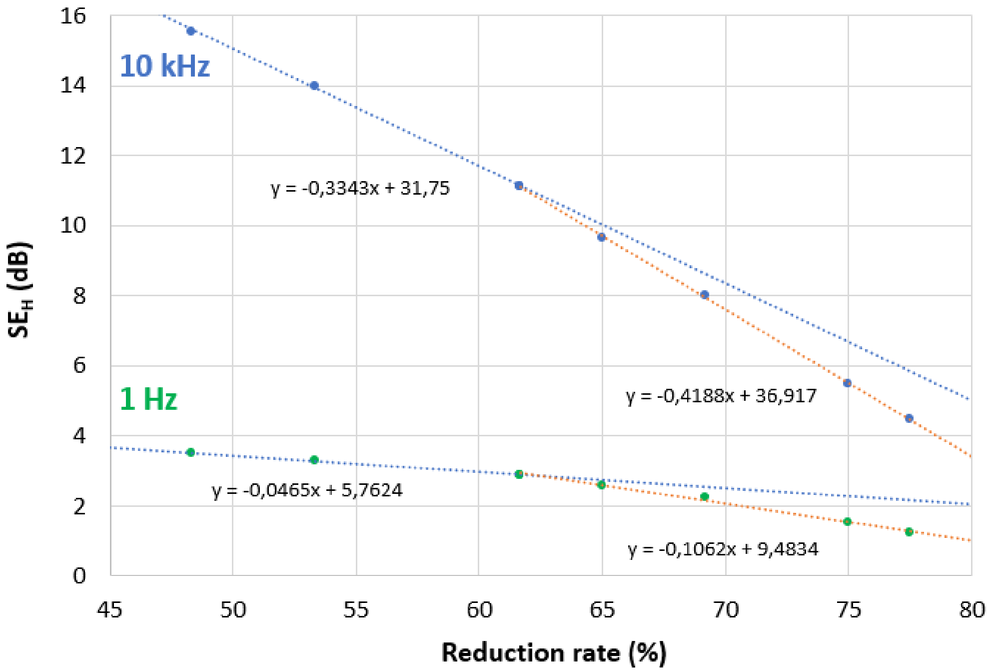

Figure 19: Numerical impact of fragmentation on $SE_H$ for 1 Hz and 10 kHz

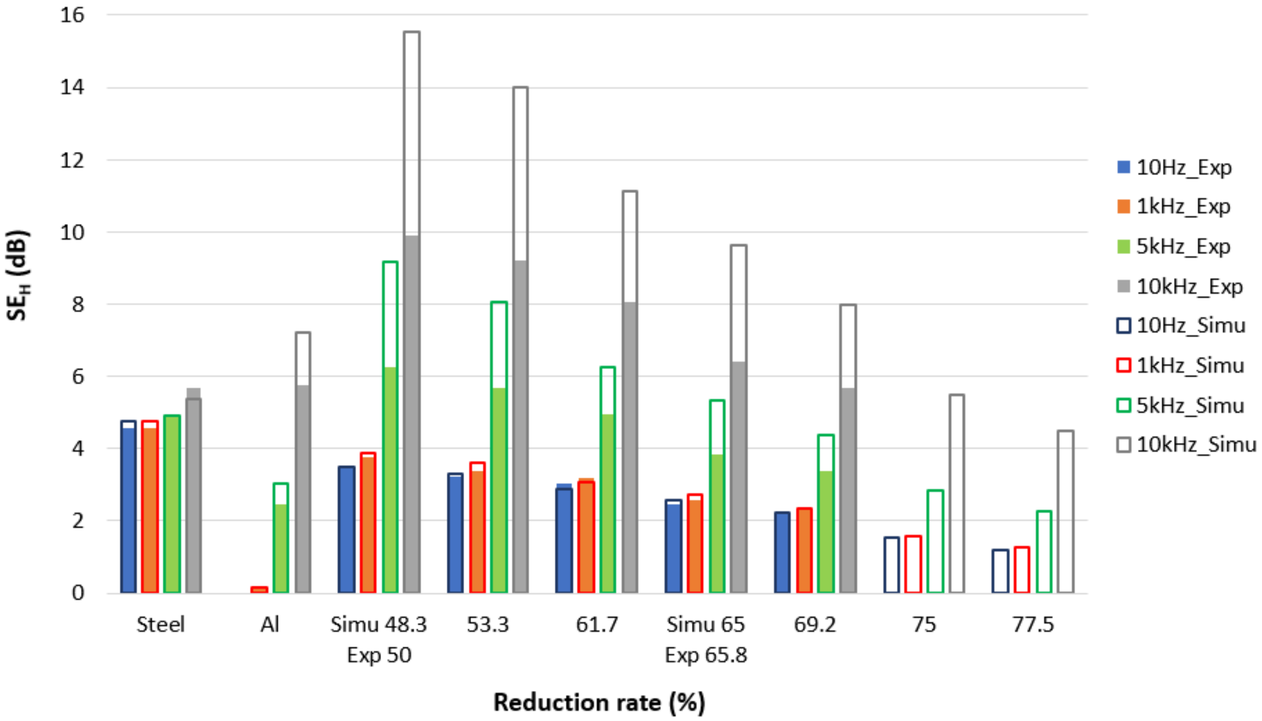

Figure 20: Comparison between experimental and numerical magnetic shielding effectiveness of 3x3 $cm^2$ samples

## List of Tables

Table 1: Chemical compositions (%wt) of Al and steel sheets

| **Al8011** | | | | | | | | |
|---|---|---|---|---|---|---|---|---|
| %Al | %Fe | %Si | %Mn | %Zn | %Cu | %Ti | %Cr | %Mg |
| Bal. | 0.6-1 | 0.5-0.9 | ≤0.2 | ≤0.1 | ≤0.1 | ≤0.08 | ≤0.05 | ≤0.05 |
| **DC01 steel** | | | | | | | | |
| | %Fe | %C | %Mn | %P | %S | %Si | %Al | |
| | Bal. | ≤0.12 | ≤0.6 | ≤0.045 | ≤0.045 | ≤0.03 | ≤0.02 | |